Progress In Electromagnetics Research B, Vol. 95, 123–140, 2022

The Role of Jordan Blocks in the MoT-Scheme Time Domain EFIE Linear-in-Time Solution Instability

Petrus W. N. van Diepen[1, *], Roeland J. Dilz[1], Adrianus P. M. Zwamborn[2], and Martijn C. van Beurden[1]

Abstract—The marching-on-in-time electric field integral equation (MOT-EFIE) and the marching-on-in-time time differentiated electric field integral equation (MOT-TDEFIE) are based on Rao-Wilton-Glisson (RWG) spatial discretization. In both formulations we employ the Dirac-delta temporal testing functions; however, they differ in temporal basis functions, i.e., hat and quadratic spline basis functions. These schemes suffer from linear-in-time solution instability. We analyze the corresponding companion matrices using projection matrices and prove mathematically that each independent solenoidal current density corresponds to a Jordan block of size two. In combination with Lidskii-Vishik-Lyusternik perturbation theory we find that finite precision causes these Jordan block eigenvalues to split, and this is the root cause of the instability of both schemes. The split eigenvalues cause solutions with exponentially increasing magnitudes that are initially observed as constant and/or linear-in-time, yet these become exponentially increasing at discrete time steps beyond the inverse square root of the error due to finite precision, i.e., approximately after one hundred million discrete time steps in double precision arithmetic. We provide numerical evidence to further illustrate these findings.

1. INTRODUCTION

An important next step in the field of computational electromagnetics (CEM) is the application of Maxwell solvers to multiphysics problems [1]. Maxwell solvers such as the time domain finite element method (TDFEM) and the finite difference time domain (FDTD) method are popular choices for multiphysics simulations dealing with electromagnetics [1, 2]. Alternative Maxwell solvers based on a Green function are time domain surface integral equations (TDSIEs). The TDSIEs have two major advantages over TDFEM and FDTD [3]: 1) owing to the Green function, TDSIEs have incorporated radiation conditions, whereas TDFEM and FDTD require proper truncation of the computational domain; 2) TDSIEs require discretization of only the wave propagation media boundaries, whereas TDFEM and FDTD require discretization of the full computational domain. These advantages could reduce the computational domain and therefore computational complexity of multiphysics solvers by replacing TDFEM and FDTD with TDSIEs as the Maxwell solver [4].

The best TDSIE formulation to use depends on the wave propagation medium [5]. To include perfect electric conductors (PECs) in a multiphysics material library, the Marching-on-in-Time Time Domain Electric Field Integral Equation (MOT-EFIE) solver and its time differentiated version (MOT-TDEFIE) would be one of the most compact TDSIE representation of the electromagnetic wave propagation. The MOT-(TD)EFIE solvers have the advantage that the unknowns at each time step only depend on the unknowns found in previous time steps [6]. Research over the years has focused on improving the

Received 2 March 2022, Accepted 11 May 2022, Scheduled 20 May 2022

* Corresponding author: Petrus Wilhelmus Nicolaas van Diepen (p.w.n.v.diepen@tue.nl).

[1] Department of Electrical Engineering, Eindhoven University of Technology, The Netherlands. [2] TNO Defence, Safety and Security, The Hague, The Netherlands.

speed and stability of the MOT-(TD)EFIE solver. A comprehensive list of speed improvements for the MOT-(TD)EFIE solver can be found in [5].

The stability improvements of the MOT-(TD)EFIE solver focus on two types of solution instability [7]: numerical instability, i.e., solution instability due to improper discretization, and spectral instability, i.e., instability of the solutions residing in the null space of the continuous (TD)EFIE operator. Major breakthroughs in removing the numerical instabilities in the MOT-(TD)EFIE solver are the exact integration techniques [8, 9] and a correct temporal discretization [10]. The MOT-(TD)EFIE design by Van 't Wout et al. [9] incorporates both numerical stabilization techniques, and it is recognized that their implementation suffers from what is known as linear-in-time solution instability. The linear-in-time solution instability is a spectral instability as numerically determined in [11]. Methods such as the combined field integral equation (CFIE) [11], inclusion of the normal magnetic field [12], dottrick Calderón preconditioned EFIE [7, 13], and the quasi-Helmholtz projectors to integrate loop and differentiate star currents in time [14] or in the Laplace-domain [15] are all designed to reduce the size of the continuous (TD)EFIE null space and deal with this linear-in-time solution instability.

Although the source of the linear-in-time solution instability is found to be the null space of the continuous (TD)EFIE, the work in [11] does not specify why the null space manifests itself as a linear-in-time solution. This question is partially answered in [7], with the companion matrix stability analysis [16] of the MOT-(TD)EFIE. In [7], the authors suspect that dimension two Jordan blocks occur in the companion matrix representation of the MOT-scheme related to the solutions in the null space of the continuous (TD)EFIE and that the Jordan blocks are the cause of the linear-in-time instability.

Here, we take a closer look at the conjecture presented in [7] and demonstrate that Jordan blocks of dimension two appear both in the MOT-EFIE and the MOT-TDEFIE companion matrix and are caused by the combination of basis and testing functions in both space and time. Finite precision effects in the representation will then lead to a splitting of these Jordan blocks that consequentially introduce exponentially increasing solution magnitudes that initially appear as constant or linear-in-time increasing magnitudes.

This paper is organized as follows. In Section 2, we review the formulation of the EFIE and TDEFIE, discuss their respective null spaces, and give the traditional discretizations that result in MOT-schemes. In Section 3, we perform a companion-matrix stability analysis of the MOT-(TD)EFIE to identify the Jordan blocks and include the effect of finite precision on the stability of the MOT-(TD)EFIE scheme. In Section 4, we validate our findings with numerical examples. We present our conclusions in Section 5.

2. FORMULATION

A perfect electric conductive (PEC) surface, Γ, resides in a homogeneous background medium with permittivity ε_0 and permeability μ_0 and resulting electromagnetic wave propagation speed $c_0 = 1/\sqrt{\varepsilon_0\mu_0}$. The incident electric field $\mathbf{E}_i(\mathbf{r}, t)$ will reach the surface Γ after $t = 0$. The time-domain electric field integral equation (EFIE) defined on Γ is given by [6],

$$\hat{\mathbf{n}} \times \hat{\mathbf{n}} \times \mathbf{E}_i(\mathbf{r}, t) = \hat{\mathbf{n}} \times \hat{\mathbf{n}} \times \int_\Gamma \mu_0 \frac{\dot{\mathbf{J}}_s(\mathbf{r}', \tau)}{4\pi R} \, \mathrm{d}A' - \hat{\mathbf{n}} \times \hat{\mathbf{n}} \times \nabla \int_\Gamma \frac{1}{\varepsilon_0} \frac{\int_{-\infty}^{\tau} \nabla'_s \cdot \mathbf{J}_s(\mathbf{r}', \bar{t}) \, \mathrm{d}\bar{t}}{4\pi R} \, \mathrm{d}A', \qquad (1)$$

where $(\mathbf{r}, t)$ are the observer space-time coordinates; $(\mathbf{r}', t')$ are the source space-time coordinates; $R = |\mathbf{r} - \mathbf{r}'|$ is the distance between source and observer; $\tau = t - \frac{R}{c_0}$ is the retarded time function; $\mathbf{J}_s$ is the surface current density on the surface Γ; $\dot{\mathbf{J}}_s$ is the derivative of $\mathbf{J}_s$ with respect to τ; $\nabla'_s \cdot$ is the surface divergence operator with respect to the source coordinates $\mathbf{r}'$; ∇ is the gradient operator with respect to the observer coordinates; $\hat{\mathbf{n}}$ denotes the unit vector normal to the boundary Γ; and $\mathrm{d}A'$ is the infinitesimal area element over the source coordinates. The first surface integral on the right hand side of (1) represents the vector potential, and the second surface integral on the right hand side of (1) represents the scalar potential. The time-differentiated electric field integral equation (TDEFIE) defined on Γ is obtained by taking the temporal derivative of Equation (1) with respect to t.

Many mathematical steps in upcoming sections are similar for both the EFIE and TDEFIE. Hence, we will denote the similar steps as sub-equations where sub-equation (a) is the step pertaining to the EFIE, and sub-equation (b) is the step pertaining to the TDEFIE. Also, in some cases the symbols for

the EFIE and TDEFIE steps have the same meaning but different values. In that case, the TDEFIE symbol will have a ∂-superscript. If the main symbol has a ∂-superscript, a ∂-superscript is also implied for all symbols in the subscript where such a definition exists to ease the notation, e.g., $\mathbf{J}_\ell^\partial = \mathbf{J}_{\ell^\partial}^\partial$.

2.1. Continuous Null Space

The stability analysis of the MOT-(TD)EFIE scheme starts from the identification of the null space of the continuous (TD)EFIE operator. The null space consists of surface current densities that do not lose their energy through electromagnetic radiation, e.g., the EFIE null space solutions consists of solutions $\mathbf{J}_s$ for which the right-hand side of (1) is zero. In literature there is a distinction between two types of null space solutions [7]:

(i) Solutions $\mathbf{J}_s$ for which the sum of the scalar potential and vector potential in (1) equals zero, but the individual terms are not zero. These solutions $\mathbf{J}_s$ are referred to as interior resonances and only exist for closed PEC surfaces Γ.

(ii) Non-zero solutions $\mathbf{J}_s$ for which the scalar potential and vector potential in (1) are equal to zero individually. These solutions $\mathbf{J}_s$ are called the DC solutions and occur for both open and closed PEC surfaces Γ.

We focus on the null space pertaining to the DC solutions, as these have been linked to the linear-in-time solution instability [11]. Expanding the surface current density as

$$\mathbf{J}_s(\mathbf{r},t) = \mathbf{J}_r(\mathbf{r})J_t(t), \quad \mathbf{J}_s^\partial(\mathbf{r},t) = \mathbf{J}_r^\partial(\mathbf{r})J_t^\partial(t), \tag{2a,b}$$

where Equation (2a) on the left is the solution to the EFIE, and Equation (2b) on the right is the solution to the TDEFIE, then the respective DC null spaces consist of the solutions for which

$$\nabla_s \cdot \mathbf{J}_r = 0 \ \wedge \ J_t = B, \quad \nabla_s \cdot \mathbf{J}_r^\partial = 0 \ \wedge \ J_t^\partial = B + Ct, \tag{3a,b}$$

holds with arbitrary non-zero constants B and C. Both (3a) and (3b) represent solenoidal surface current densities. However, the solutions in (3a) are restricted to constant-in-time solutions, while (3b) also admits linear-in-time solutions.

2.2. Discretization

To find a numerical approximation of the solution $\mathbf{J}_s$ for the (TD)EFIE (1), the surface current density is approximated as

$$\mathbf{J}_s(\mathbf{r},t) = \sum_{m'=1}^{M}\sum_{n'=1}^{N} J_{m',n'}\mathbf{f}_{m'}(\mathbf{r})T_{n'}(t), \tag{4}$$

where $J_{m',n'}$ is an expansion coefficient, $\mathbf{f}_{m'}$ the m'-th spatial basis function defined on $\Gamma_{m'}$, and $T_{n'}$ the n'-th temporal basis function. Substituting (4) in (1), multiplying the equation with the Dirac-delta temporal test functions $\delta(t - n\Delta t)$ for $n = 1, \ldots, N$ and spatial test functions $\mathbf{f}_m(\mathbf{r})$ for $m = 1, \ldots, M$ and integrating the result over t and Γ_m, we arrive at a linear system with coefficients, i.e., matrix elements, given by the sum of the bilinear forms

$$\mathcal{A}_n(\mathbf{f}_m, \mathbf{f}_{m'}, T_{n'}) = \mu_0 \int_{\Gamma_m} \mathbf{f}_m \cdot \int_{\Gamma_{m'}} \frac{\mathbf{f}_{m'}\dot{T}_{n'}(\tau_n)}{4\pi R}\,\mathrm{d}A'\mathrm{d}A, \tag{5}$$

and

$$\phi_n(\mathbf{f}_m, \mathbf{f}_{m'}, T_{n'}) = \frac{1}{\varepsilon_0}\int_{\Gamma_m} \nabla_s \cdot \mathbf{f}_m \int_{\Gamma_{m'}} \frac{\nabla_s' \cdot \mathbf{f}_{m'} \int_{-\infty}^{\tau_n} T_{n'}(\bar{t})\mathrm{d}\bar{t}}{4\pi R}\,\mathrm{d}A'\mathrm{d}A, \tag{6}$$

where $\tau_n = \tau(n\Delta t)$ and $\dot{T}_{n'}$ is the derivative of $T_{n'}$ with respect to t. Here, $\mathcal{A}_n$ and ϕ_n are the discretized versions of the vector and scalar potential, respectively, in the right hand side of Equation (1). The combination of spatial-temporal basis and test functions is not arbitrary as the stability of the MOT-(TD)EFIE depends on it [10]. According to [10], the Rao-Wilton-Glisson (RWG) [17] functions are a proper choice for the MOT-(TD)EFIE spatial basis, $\mathbf{f}_{m'}$, and testing functions, $\mathbf{f}_m$. Although the spatial

discretization is equal for both MOT-EFIE and MOT-TDEFIE, the temporal discretization is not. The MOT-EFIE requires the hat temporal basis function [8],

$$T_{n'}(t) = \begin{cases} 1 - \left| \dfrac{t - n'\Delta t}{\Delta t} \right|, & \text{for } -\Delta t < (t - n'\Delta t) \leq \Delta t, \\ 0, & \text{otherwise,} \end{cases} \tag{7a}$$

while the MOT-TDEFIE requires the quadratic spline temporal basis function [10],

$$T^{\partial}_{n'}(t) = \begin{cases} \dfrac{1}{2}\left(\dfrac{t - n'\Delta t}{\Delta t}\right)^2 + \dfrac{t - n'\Delta t}{\Delta t} + \dfrac{1}{2}, & \text{for } -\Delta t < (t - n'\Delta t) \leq 0, \\ -\left(\dfrac{t - n'\Delta t}{\Delta t}\right)^2 + \dfrac{t - n'\Delta t}{\Delta t} + \dfrac{1}{2}, & \text{for } 0 < (t - n'\Delta t) \leq \Delta t, \\ \dfrac{1}{2}\left(\dfrac{t - n'\Delta t}{\Delta t}\right)^2 - 2\dfrac{t - n'\Delta t}{\Delta t} + 2, & \text{for } \Delta t < (t - n'\Delta t) \leq 2\Delta t, \\ 0, & \text{otherwise.} \end{cases} \tag{7b}$$

These choices of spatial-temporal discerizations result in the MOT-EFIE (8a) and MOT-TDEFIE (8b),

$$\mathbf{Z}_0 \mathbf{J}_n = \mathbf{E}_{i,n} - \sum_{n'=n-\ell}^{n-1} \mathbf{Z}_{n-n'} \mathbf{J}_{n'} - \mathbf{Z}_{\text{tail}} \sum_{n'=1}^{n-\ell-1} \mathbf{J}_{n'}, \quad \mathbf{Z}^{\partial}_0 \mathbf{J}^{\partial}_n = \mathbf{E}^{\partial}_{i,n} - \sum_{(n')=n-\ell^{\partial}}^{n-1} \mathbf{Z}^{\partial}_{n-n'} \mathbf{J}^{\partial}_{n'}. \tag{8a,b}$$

The matrices $\mathbf{Z}_{n-n'}$ and $\mathbf{Z}^{\partial}_{n-n'}$ are called the interaction matrices and have to be precomputed for different values of $n - n'$ up to, see [11],

$$\ell = \left\lceil \frac{R_{\max}}{c\Delta t} \right\rceil + 1, \quad \ell^{\partial} = \left\lceil \frac{R_{\max}}{c\Delta t} \right\rceil + 2, \tag{9a,b}$$

where $R_{\max}$ is the largest possible separation between observer and source point on the discretized surface Γ. The interaction matrix elements at row m and column m' are defined as

$$Z_{n-n'}(m, m') = \mathcal{A}_n(\mathbf{f}_m, \mathbf{f}_{m'}, T_{n'}) + \phi_n(\mathbf{f}_m, \mathbf{f}_{m'}, T_{n'}), \quad Z_{\text{tail}} = \dot{\phi}_n(\mathbf{f}_m, \mathbf{f}_{m'}, \Delta t), \tag{10a}$$

$$Z^{\partial}_{n-n'}(m, m') = \dot{\mathcal{A}}_n(\mathbf{f}_m, \mathbf{f}_{m'}, T^{\partial}_{n'}) + \dot{\phi}_n(\mathbf{f}_m, \mathbf{f}_{m'}, T^{\partial}_{n'}), \tag{10b}$$

where $\dot{\mathcal{A}}_n$ and $\dot{\phi}_n$ are the derivatives of $\mathcal{A}_n$ (5) and ϕ_n (6) with respect to t.

3. COMPANION MATRIX STABILITY ANALYSIS OF THE MOT-EFIE AND MOT-TDEFIE

The stability of the MOT-(TD)EFIE can be analyzed using the corresponding companion matrix [16]. As we will use the companion matrix extensively in the next sections, we will first summarize how the companion matrix relates to the stability performance of the MOT-(TD)EFIE.

In the companion-matrix stability analysis, we consider the MOT-(TD)EFIE without excitation, i.e., $\mathbf{E}_{i,n} = \mathbf{E}^{\partial}_{i,n} = \mathbf{0}\ \forall\ n$ in Equation (8). The MOT-EFIE solution $\mathbf{J}_n$ then depends on $\mathbf{J}_{n'}$ for $n' = n-1, \ldots, n-\ell$ and the sum $\sum_{n'=1}^{n-\ell-1} \mathbf{J}_{n'}$. The MOT-TDEFIE solution $\mathbf{J}^{\partial}_n$ then depends on $\mathbf{J}^{\partial}_{n'}$ for $n' = n-1, \ldots, n-\ell^{\partial}$. Column concatenation of these current density vectors will result in what is known as the composite current density vector [16],

$$\mathbf{C}_n = \left[\mathbf{J}_{n-1}\ \cdots\ \mathbf{J}_{n-\ell}\ \textstyle\sum_{i=1}^{n-\ell-1} \mathbf{J}_i\right]^T, \quad \mathbf{C}^{\partial}_n = \left[\mathbf{J}^{\partial}_{n-1}\ \cdots\ \mathbf{J}^{\partial}_{n-\ell+1}\ \mathbf{J}^{\partial}_{n-\ell}\right]^T. \tag{11a,b}$$

As $\ell^{\partial} = \ell + 1$, see (9), the dimensions of $\mathbf{C}_n$ and $\mathbf{C}^{\partial}_n$ are equal for a given RWG discretization. The companion matrix, $\mathbf{Q}$, expresses the relation between two consecutive composite current density vectors, i.e.,

$$\mathbf{C}_n = \mathbf{Q}\mathbf{C}_{n-1} = \mathbf{Q}^k \mathbf{C}_{n-k}, \quad \mathbf{C}^{\partial}_n = \mathbf{Q}^{\partial}\mathbf{C}^{\partial}_{n-1} = \left(\mathbf{Q}^{\partial}\right)^k \mathbf{C}^{\partial}_{n-k}, \tag{12a,b}$$

and is consequently given by,

$$\mathbf{Q} = \begin{bmatrix} \mathbf{Q}_1 & \mathbf{Q}_2 & \cdots & \cdots & \mathbf{Q}_\ell & \mathbf{Q}_{\text{tail}} \\ \mathbf{I} & \mathbf{0} & \cdots & \cdots & \mathbf{0} & \mathbf{0} \\ \mathbf{0} & \mathbf{I} & \ddots & & \vdots & \vdots \\ \vdots & \ddots & \ddots & \ddots & \vdots & \vdots \\ \vdots & & \ddots & \mathbf{I} & \mathbf{0} & \mathbf{0} \\ \mathbf{0} & \cdots & \cdots & \mathbf{0} & \mathbf{I} & \mathbf{I} \end{bmatrix}, \quad \mathbf{Q}^\partial = \begin{bmatrix} \mathbf{Q}_1^\partial & \mathbf{Q}_2^\partial & \cdots & \cdots & \mathbf{Q}_{\ell-1}^\partial & \mathbf{Q}_\ell^\partial \\ \mathbf{I} & \mathbf{0} & \cdots & \cdots & \mathbf{0} & \mathbf{0} \\ \mathbf{0} & \mathbf{I} & \ddots & & \vdots & \vdots \\ \vdots & \ddots & \ddots & \ddots & \vdots & \vdots \\ \vdots & & \ddots & \mathbf{I} & \mathbf{0} & \mathbf{0} \\ \mathbf{0} & \cdots & \cdots & \mathbf{0} & \mathbf{I} & \mathbf{0} \end{bmatrix}, \tag{13a,b}$$

where for $i = 1, \ldots, \ell$ or $i = 1, \ldots, \ell^\partial$

$$\mathbf{Q}_i = -\mathbf{Z}_0^{-1}\mathbf{Z}_i \quad \mathbf{Q}_{\text{tail}} = -\mathbf{Z}_0^{-1}\mathbf{Z}_{\text{tail}}, \quad \mathbf{Q}_i^\partial = -\left(\mathbf{Z}_0^\partial\right)^{-1}\mathbf{Z}_i^\partial. \tag{14a,b}$$

So, given an initial composite current density vector, one can compute the resulting composite current density vector after any number of time steps k using the companion matrix to the power k. Therefore, the stability of the MOT-EFIE and MOT-TDEFIE depends on boundedness of the matrix elements in $\mathbf{Q}^k$ and $(\mathbf{Q}^\partial)^k$, respectively.

The boundedness of the companion matrix power elements can be analyzed using the Jordan Canonical Form (JCF) [7, 18],

$$\mathbf{Q} = \mathbf{T}\mathbf{\Lambda}\mathbf{T}^{-1} \Leftrightarrow (\mathbf{Q})^k = \mathbf{T}\left(\mathbf{\Lambda}\right)^k\mathbf{T}^{-1}, \quad \mathbf{Q}^\partial = \mathbf{T}^\partial\mathbf{\Lambda}^\partial\left(\mathbf{T}^\partial\right)^{-1} \Leftrightarrow \left(\mathbf{Q}^\partial\right)^k = \mathbf{T}^\partial\left(\mathbf{\Lambda}^\partial\right)^k\left(\mathbf{T}^\partial\right)^{-1}, \tag{15a,b}$$

where $\mathbf{\Lambda}$ and $\mathbf{\Lambda}^\partial$ are Jordan matrices, i.e., a block-diagonal matrix, filled with the Jordan blocks $\mathbf{\Omega}_i$ and $\mathbf{\Omega}_i^\partial$, respectively. The matrix $\mathbf{T}$ represents a complete vector basis for $\mathbb{R}^{M(\ell+1)}$, and $\mathbf{T}^\partial$ represents a complete vector basis $\mathbb{R}^{M\ell^\partial}$. Each Jordan block is coupled to an eigenvalue of the associated companion-matrix, i.e., λ_i are the eigenvalues of $\mathbf{Q}$, and λ_i^∂ are the eigenvalues of $\mathbf{Q}^\partial$. The number of Jordan blocks pertaining to a single eigenvalue is equal to the geometric multiplicity of the eigenvalue, while the size of these Jordan blocks depends on the algebraic multiplicity of the eigenvalue as the sum of Jordan block dimensions is equal to the algebraic multiplicity [18]. The boundedness of $\mathbf{Q}^k$ depends on the boundedness of the elements of all $\mathbf{\Omega}_i^k$. As long as all the associated eigenvalues have a magnitude smaller than one, i.e., $|\lambda_i| < 1$, the Jordan block matrix powers remain bounded for all k independent of the size of the associated Jordan block. On the contrary, if a single eigenvalue has a magnitude larger than one, i.e., $|\lambda_i| > 1$, the associated Jordan block matrix power upper triangular elements will increase exponentially with k independent of the size of the associated Jordan block. However, if $|\lambda_i| = 1$, the associated Jordan block matrix power elements above its diagonal will increase binomially with respect to k [18]. In that case, the Jordan block matrix power is bounded if and only if all the associated Jordan blocks have dimension one. The above also holds for the Jordan blocks $\mathbf{\Omega}_i^\partial$ with eigenvalues λ_i^∂. Hence, the stability of the MOT-EFIE and MOT-TDEFIE depends not only on the magnitude of the eigenvalues of the companion matrix but also on the dimension of the Jordan blocks with $|\lambda| = 1$, as already suggested in [7].

3.1. Solenoidal and Non-Solenoidal Current Density in the MOT-(TD)EFIE

The surface current densities that belong to the DC null space (3) give rise to $|\lambda| = 1$ eigenvalues in the companion matrix eigenvalue spectrum [7]. To understand how the DC null space solutions affect the stability of the MOT-(TD)EFIE solution, we analyze how these solutions manifest themselves in the companion matrix. To do that, we distinguish between RWG combinations that represent solenoidal current densities and RWG combinations that represent non-solenoidal current densities.

The surface current density is represented using M linearly independent RWG basis functions as in (4). Linear combinations of the RWG basis functions can be constructed to generate a basis consisting of Θ linearly independent solenoidal, $\boldsymbol{\theta}_m(\mathbf{r})$, and Ψ linearly independent non-solenoidal, $\boldsymbol{\psi}_p(\mathbf{r})$, basis functions, i.e.,

$$\left[\boldsymbol{\theta}_1, \ldots, \boldsymbol{\theta}_\Theta, \boldsymbol{\psi}_1, \ldots, \boldsymbol{\psi}_\Psi\right]^T = \mathbf{P}\left[\mathbf{f}_1, \ldots, \mathbf{f}_M\right]^T. \tag{16}$$

where $\Theta + \Psi = M$ and $\nabla \cdot \boldsymbol{\theta}_m = 0$ and $\nabla \cdot \boldsymbol{\psi}_p \neq 0$ holds for the new basis functions. The matrix $\mathbf{P}$ is called a projection matrix [14]. The process is reversible, i.e., $\mathbf{P}$ is invertible, and a unique linear combination of $\boldsymbol{\theta}_m$ and $\boldsymbol{\psi}_p$ basis functions represents each RWG basis function. Although the use of a projection matrix is similar to loop-star or loop-tree decomposition [14], they differ in the sense that the loop-star/tree decomposition only includes local loops while the solenoidal basis functions, $\boldsymbol{\theta}_m$, include both local and global loops, where global loops occur, e.g., on the surface of a torus.

Multiplication of $\mathbf{P}$ with the interaction matrices results in a new interaction matrix where $\boldsymbol{\theta}_m$ and $\boldsymbol{\psi}_p$ are the spatial testing functions. Similarly, multiplication of interaction matrices with $\mathbf{P}^T$ results in a new interaction matrix with $\boldsymbol{\theta}_m$ and $\boldsymbol{\psi}_p$ as the spatial basis functions. So, the interaction matrices with solenoidal and non-solenoidal basis and testing functions are based on the interaction matrices with RWG basis and testing functions and are defined as the block matrices

$$\mathbf{P}\mathbf{Z}_{n-n'}\mathbf{P}^T = \begin{bmatrix} \mathbf{Z}_{n-n'}^{\boldsymbol{\theta}\boldsymbol{\theta}} & \mathbf{Z}_{n-n'}^{\boldsymbol{\theta}\boldsymbol{\psi}} \\ \mathbf{Z}_{n-n'}^{\boldsymbol{\psi}\boldsymbol{\theta}} & \mathbf{Z}_{n-n'}^{\boldsymbol{\psi}\boldsymbol{\psi}} \end{bmatrix}, \quad \mathbf{P}\mathbf{Z}_{\text{tail}}\mathbf{P}^T = \begin{bmatrix} \mathbf{0} & \mathbf{0} \\ \mathbf{0} & \mathbf{Z}_{\text{tail}}^{\boldsymbol{\psi}\boldsymbol{\psi}} \end{bmatrix}, \tag{17a}$$

$$\mathbf{P}\mathbf{Z}_{n-n'}^{\partial}\mathbf{P}^T = \begin{bmatrix} \mathbf{Z}_{n-n'}^{\partial\boldsymbol{\theta}\boldsymbol{\theta}} & \mathbf{Z}_{n-n'}^{\partial\boldsymbol{\theta}\boldsymbol{\psi}} \\ \mathbf{Z}_{n-n'}^{\partial\boldsymbol{\psi}\boldsymbol{\theta}} & \mathbf{Z}_{n-n'}^{\partial\boldsymbol{\psi}\boldsymbol{\psi}} \end{bmatrix}, \tag{17b}$$

where the elements of the block matrices are defined as

$$Z_{n-n'}^{\boldsymbol{\theta}\boldsymbol{\theta}}(m,m') = \mathcal{A}_n(\boldsymbol{\theta}_m, \boldsymbol{\theta}_{m'}, T_{n'}), \quad Z_{n-n'}^{\partial\boldsymbol{\theta}\boldsymbol{\theta}}(m,m') = \dot{\mathcal{A}}_n(\boldsymbol{\theta}_m, \boldsymbol{\theta}_{m'}, T_{n'}^{\partial}), \tag{18a,b}$$

$$Z_{n-n'}^{\boldsymbol{\theta}\boldsymbol{\psi}}(m,p') = \mathcal{A}_n(\boldsymbol{\theta}_m, \boldsymbol{\psi}_{p'}, T_{n'}), \quad Z_{n-n'}^{\partial\boldsymbol{\theta}\boldsymbol{\psi}}(m,p') = \dot{\mathcal{A}}_n(\boldsymbol{\theta}_m, \boldsymbol{\psi}_{p'}, T_{n'}^{\partial}), \tag{19a,b}$$

$$Z_{n-n'}^{\boldsymbol{\psi}\boldsymbol{\theta}}(p,m') = Z_{n-n'}^{\boldsymbol{\theta}\boldsymbol{\psi}}(m,p'), \quad Z_{n-n'}^{\partial\boldsymbol{\psi}\boldsymbol{\theta}}(p,m') = Z_{n-n'}^{\partial\boldsymbol{\theta}\boldsymbol{\psi}}(m,p'), \tag{20a,b}$$

$$Z_{n-n'}^{\boldsymbol{\psi}\boldsymbol{\psi}}(p,p') = \mathcal{A}_n(\boldsymbol{\psi}_p, \boldsymbol{\psi}_{p'}, T_{n'}) + \phi_n(\boldsymbol{\psi}_p, \boldsymbol{\psi}_{p'}, T_{n'}), \tag{21a}$$

$$Z_{n-n'}^{\partial\boldsymbol{\psi}\boldsymbol{\psi}}(p,p') = \dot{\mathcal{A}}_n(\boldsymbol{\psi}_p, \boldsymbol{\psi}_{p'}, T_{n'}^{\partial}) + \dot{\phi}_n(\boldsymbol{\psi}_p, \boldsymbol{\psi}_{p'}, T_{n'}^{\partial}), \tag{21b}$$

$$Z_{\text{tail}}^{\boldsymbol{\psi}\boldsymbol{\psi}}(p,p') = \dot{\phi}(\boldsymbol{\psi}_p, \boldsymbol{\psi}_{p'}, \Delta t). \tag{22}$$

By replacing $\mathbf{Q}_i$ and $\mathbf{Q}_{\text{tail}}$ in (13a) by

$$\mathbf{Q}_{P,i} = -\left(\mathbf{P}\mathbf{Z}_0\mathbf{P}^{\mathrm{T}}\right)^{-1}\mathbf{P}\mathbf{Z}_i\mathbf{P}^{\mathrm{T}} \text{ and } \mathbf{Q}_{P,\text{tail}} = -\left(\mathbf{P}\mathbf{Z}_0\mathbf{P}^T\right)^{-1}\mathbf{P}\mathbf{Z}_{\text{tail}}\mathbf{P}^T, \tag{23a}$$

respectively, we can define the projected MOT-EFIE companion matrix $\mathbf{Q}_P$. Likewise, we can define the projected MOT-TDEFIE companion matrix $\mathbf{Q}_P^{\partial}$ by replacing $\mathbf{Q}_i^{\partial}$ in (13b) with

$$\mathbf{Q}_{P,i}^{\partial} = -\left(\mathbf{P}\mathbf{Z}_0^{\partial}\mathbf{P}^T\right)^{-1}\mathbf{P}\mathbf{Z}_i^{\partial}\mathbf{P}^T. \tag{23b}$$

The projected companion matrices are similar to the original companion matrices, i.e.,

$$\mathbf{Q} = \mathbf{D}_{\mathbf{P}^T}\mathbf{Q}_P\mathbf{D}_{\mathbf{P}^T}^{-1}, \quad \mathbf{Q}^{\partial} = \mathbf{D}_{\mathbf{P}^T}\mathbf{Q}_P^{\partial}\mathbf{D}_{\mathbf{P}^T}^{-1}, \tag{24a,b}$$

where $\mathbf{D}_{\mathbf{P}^T}$ is a block-diagonal matrix with $\mathbf{P}^T$ as blocks. These block matrices introduce only a similarity transformation in the above expressions, and therefore the Jordan matrices in the JCF of the companion matrix and the projected companion matrix are the same.

To find the Jordan matrix, we require the eigenvalues and eigenvectors of the projected companion matrix. The eigenvalues can be found by solving the characteristic polynomial equations $\det(\mathbf{Q}_P - \lambda\mathbf{I}) = 0$ and $\det(\mathbf{Q}_P^{\partial} - \lambda^{\partial}\mathbf{I}) = 0$. In Appendix A we have worked out these characteristic polynomials, and regarding the roots for the case $\lambda = 1$ we come to the conclusion that both can be simplified to the polynomial

$$\left((\lambda^{(\partial)} - 1)^2\right)^{\Theta} = 0. \tag{25}$$

The power Θ in the above equation implies that every basis function $\boldsymbol{\theta}_m$ in both $\mathbf{Q}_P$ and $\mathbf{Q}_P^{\partial}$ is associated with an eigenvalue $\lambda = 1$. The power of two in the above equation implies that each of these eigenvalues has an algebraic multiplicity of two. In Appendix B we derive expressions for the eigenvectors associated with $\lambda = 1$ and find that the geometric multiplicity of $\lambda = 1$ is Θ, indicating a Jordan block of a dimension larger than one. Furthermore, in Appendix B we also show that each eigenvector is associated with a unique generalized eigenvector. This implies that each of the Θ Jordan blocks is associated with one eigenvector and one generalized eigenvector. Therefore, the dimension of all Θ Jordan blocks for $\lambda = 1$ equals two.

Due to the similarity between the companion matrix and the projected companion matrix (24), we can conclude that every linear combination of RWGs representing a linearly independent solenoidal basis function is associated with $\lambda = 1$ with an algebraic multiplicity of two and geometric multiplicity of one and a Jordan block of dimension two in both the MOT-EFIE and MOT-TDEFIE companion matrix JCF-forms.

3.2. The Effect of Finite Precision on the MOT-(TD)EFIE Stability

The analysis in Section 3.1 does not hold when including finite precision as this will perturb the interaction matrix values from their theoretical values, and the required recurrence relation (A6) is lost. The effect of perturbations on the companion-matrix element values on the Jordan matrix $\boldsymbol{\Lambda}$ (15) can be understood using the Lidskii-Vishik-Lyusternik perturbation theory [19]. The Lidskii-Vishik-Lyusternik perturbation theory states that a perturbation of magnitude ϵ to a matrix with arbitrary Jordan structures splits the eigenvalues of each individual Jordan block of dimension n in n shifted eigenvalues where the shift is in the order of $\mathcal{O}(\epsilon^{\frac{1}{n}})$ [19]. Each shifted eigenvalue is now part of a one-dimensional Jordan block. In our case, the Jordan block is of dimension $n = 2$. Consequently, the two eigenvalues of the dimension-two Jordan blocks for $\lambda = 1$ split into

- the eigenvalues $\lambda_1 = 1 + \alpha_1$ and $\lambda_2 = 1 + \alpha_2$ if $\alpha_1, \alpha_2 \in \mathbb{R}$, where $|\alpha_1|$ and $|\alpha_2|$ are of the order $\mathcal{O}(\sqrt{\epsilon})$, or,
- the eigenvalues $\lambda_1 = 1 + \alpha$ and $\lambda_2 = 1 + \alpha^*$ if $\alpha \in \mathbb{C}$, where $|\alpha|$ is of the order $\mathcal{O}(\sqrt{\epsilon})$ and α^* is the complex conjugate of α.

Although α can be complex, the eigenvalues come in complex conjugated pairs, which is what should be expected for a real-valued matrix. So, due to finite precision, we will lose the dimension-two Jordan blocks in the JCF of the companion matrices, and we are left with a diagonal Jordan matrix $\boldsymbol{\Lambda}$ with eigenvalues λ on the diagonal.

The composite current density vector $\mathbf{C}_n$ at a future time step k can now be determined via the matrix multiplication $\mathbf{T}\boldsymbol{\Lambda}^k\mathbf{T}^{-1}$ (15). However, the perturbations will also change the matrices $\mathbf{T}$ in an unpredictable manner. Therefore, the only conclusion that we can draw is that the surface current densities in $\mathbf{C}_n$ will depend on a linear combination of the 2Θ shifted eigenvalues $\lambda_m^k = (1 + \alpha_m)^k$,

$$\sum_m^{2\Theta} \beta_m \left(1 + \alpha_m\right)^k = \sum_m^{2\Theta} \beta_m + k \sum_m^{2\Theta} \alpha_m \beta_m + \frac{k(k-1)}{2} \sum_m^{2\Theta} \alpha_m^2 \beta_m + \ldots, \tag{26}$$

where β_m results from the matrix multiplication $\mathbf{T}\boldsymbol{\Lambda}^k\mathbf{T}^{-1}$. If α_m and β_m are complex numbers, the complex conjugates are also present in (26). Although all $(1 + \alpha_m)^k$ are exponentially increasing in magnitude with k, linear combinations of the $(1+\alpha_m)^k$ eigenvalues permit different magnitude increases in $\mathbf{C}_n$:

(i) For $k|\alpha_m| \ll 1 \ \forall \ m$, the most dominant term in (26) is the first term, and $\mathbf{C}_n$ includes surface current density magnitudes observed as constant in time;

(ii) For $k|\alpha_m| \geq 1 \ \forall \ m$, the first term is not the dominant term in (26), and $\mathbf{C}_n$ includes surface current densities with magnitudes that increase exponentially with time. Due to the complex-conjugated pairs in the sequence α_m, some of the allowed exponentially increasing surface current densities oscillate;

(iii) In the transition region between points (i) and (ii), there might exist values of k where the second term is the dominant term in (26), and $\mathbf{C}_n$ includes surface current densities with magnitudes that are observed as linearly increasing with time. In the same transition region, the third or higher order terms in (26) can also become dominant for values of k, although this remains less likely as these values are proportional to powers of α_m, which are very small. In that case, the current density increases in magnitude as a higher order polynomial.

Although the surface current density magnitude can be observed as constant and/or linear with respect to the discrete time step k, for values of k large enough, such that $k|\alpha_m| \geq 1 \; \forall \; m$, the surface current density magnitude will always increase exponentially with k.

4. NUMERICAL EVIDENCE

In Section 3, we have proven that each linearly-independent solenoidal surface current density supported by the MOT-EFIE and MOT-TDEFIE discretizations introduces a dimension-two Jordan block in their respective companion matrices. Finite-precision effects in the representation will then lead to a splitting of these Jordan blocks that subsequently introduce solutions with exponentially increasing magnitudes that initially appear as constant or linear-in-time increasing magnitudes. We continue by providing numerical examples to illustrate that the MOT-EFIE and MOT-TDEFIE behaviors are in line with the theory provided in Section 3. We will address the following four assertions with numerical evidence.

(i) In Section 4.1 we show that we have a correct implementation of the MOT-EFIE and MOT-TDEFIE solvers as proposed in [9];

(ii) In Section 4.2 we provide evidence that for each linear combination of RWGs representing a linearly independent solenoidal surface current density, we observe two eigenvalues close to $\lambda = 1$ in the MOT-EFIE and MOT-TDEFIE companion matrices;

(iii) In Section 4.3 we provide evidence that the eigenvalues close to $\lambda = 1$ have an offset α, where $|\alpha|$ is proportional to the square root of the precision with which the interaction matrix was calculated. Furthermore, we show that finite-precision arithmetic causes the offset α in the MOT-EFIE and MOT-TDEFIE implementations;

(iv) In Section 4.4 we provide evidence that the presence of Jordan blocks in combination with finite-precision effects causes exponentially increasing solutions, which initially appear as constant and/or linear-in-time increasing solutions.

4.1. MOT-EFIE and MOT-TDEFIE Implementation

For assertion (i), we compare our surface current density results to the MOT-TDEFIE results published by Vechinski and Rao [20]. Although the MOT-TDEFIE implementation in [20] suffers from late-time instability, most likely due to a low-accuracy interaction matrix, the results remain stable in the region of interest.

The PEC scatterers in [20] and used in our numerical validation experiment are a $4\,\mathrm{m}^2$ plate, see Figure 1(a), and a $1\,\mathrm{m}^3$ cube, see Figure 1(b). Both objects are excited by an incident $\hat{\mathbf{x}}$-polarized Gaussian plane wave travelling in the negative $\hat{\mathbf{z}}$-direction, i.e.,

$$\mathbf{E}^i(\mathbf{r},t) = \hat{\mathbf{x}}\frac{1}{\sqrt{\pi}}\exp\left(-(c_0(t-t_0)+\mathbf{r}\cdot\hat{\mathbf{z}}))^2\right)\,[\mathrm{V/m}], \tag{27}$$

where t_0 is the separation time at time $t = 0$ between the Gaussian pulse center and the coordinate system origin in lm. The unit lm in this context is known as lightmeter, i.e., the time it takes for the wave front to travel a distance of 1 m. The values for t_0 for the plate and cube are $t_0 = 6\,\mathrm{lm}$ and $t_0 = 6.5\,\mathrm{lm}$, respectively. The parameters required by the implementation in [9] are set to $\epsilon_{\mathrm{edge}} = 10^{-8}$, $\epsilon_{\mathrm{vertex}} = 10^{-8}$, a fifth order Dunavant's Gaussian quadrature rule and $\Delta t = 0.25\,\mathrm{lm}$.

The surface current densities induced by the Gaussian plane wave (27) sampled on the PEC scatterer surfaces computed using the MOT-EFIE and MOT-TDEFIE, as shown in Section 2, are shown in Figure 1. As can be seen in Figure 1, the results of our MOT-EFIE and our MOT-TDEFIE are similar, where the relative root mean square deviation of the MOT-TDEFIE solution with respect to

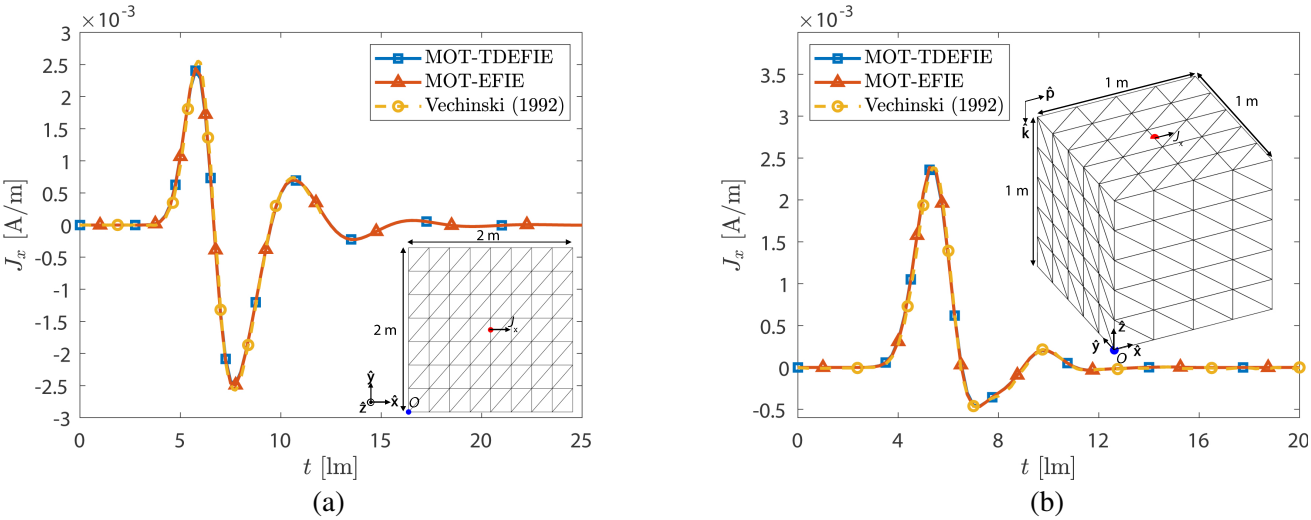

Figure 1. A comparison of the Gaussian plane-wave (27) excited surface current density solution, $J_x(t)$, of our MOT-EFIE and MOT-TDEFIE implementation with the solutions presented by Vechinski et al. [20] for (a) a $4\,\mathrm{m}^2$ PEC plate with $J_x(t) = \hat{\mathbf{x}} \cdot \mathbf{J}_s([1,1,0],t)$, and (b) a $1\,\mathrm{m}^3$ PEC cube with $J_x(t) = \hat{\mathbf{x}} \cdot \mathbf{J}_s([0.5,0.5,1],t)$. The red and blue dots in the mesh represent the sample and origin locations, respectively.

the MOT-EFIE solution is $1.18 \cdot 10^{-2}$ in Figure 1(a) and $1.24 \cdot 10^{-2}$ in Figure 1(b), indicating a correct implementation of the two solvers. Furthermore, our MOT-EFIE and MOT-TDEFIE results are similar to the surface current density solutions of the MOT-TDEFIE published in [20] that we visually sampled and plotted in Figure 1, where the relative root mean square deviation of our MOT-TDEFIE solution with respect to the MOT-TDEFIE by Vechinski an Rao solution is $6.9 \cdot 10^{-2}$ in Figure 1(a) and $6.5 \cdot 10^{-2}$ in Figure 1(b), and the relative root mean square deviation of our MOT-EFIE solution with respect to the MOT-TDEFIE by Vechinski and Rao solution is $6.2 \cdot 10^{-2}$ in Figure 1(a) and $6.4 \cdot 10^{-2}$ in Figure 1(b). The difference between our results and the results presented in [20] can be explained, as our implementation has an analytic evaluation of the underlying integrals for the potentials and their derivatives compared to the implementation in [20]. This difference in implementation results in a difference in the result but also in the stability of the two implementations. This establishes our confidence in our implementation.

4.2. Number of Jordan Block Eigenvalues

For assertion (ii), we compare the number of eigenvalues close to $\lambda = 1$ in the companion-matrix representation to the number of linear RWG combinations representing a linearly independent solenoidal current density in Figure 1. The PEC plate in Figure 1(a) is an example of an open simply connected surface for which each set of RWGs that share an interior node represents a linearly independent solenoidal surface current density [21]. We count 42 interior nodes. Therefore, we expect 84 eigenvalues close to $\lambda = 1$. The PEC cube in Figure 1(b) is an example of a closed simply connected surface for which each set of RWGs that share a node can represent a solenoidal surface current density, and the number of linearly independent sets is equal to the number of nodes minus one [21]. We count 131 nodes. Therefore, we expect 262 eigenvalues close to $\lambda = 1$.

The eigenvalues of the companion matrices based on the interaction matrices used in Figures 1(a) and 1(b) are presented in Figures 2 and 3, respectively. Similar eigenvalue distributions have been presented in literature [7, 12, 15] for the MOT-TDEFIE companion matrix corresponding to a PEC spherical scatterer. Counting the number of eigenvalues close to $\lambda = 1$, we count 84 eigenvalues in Figure 2(b) and 262 eigenvalues in Figure 3(b) for both the MOT-EFIE and MOT-TDEFIE. These numbers are in line with assertion (ii).

To illustrate that assertion (ii) also holds for non-simply connected surfaces, we have constructed

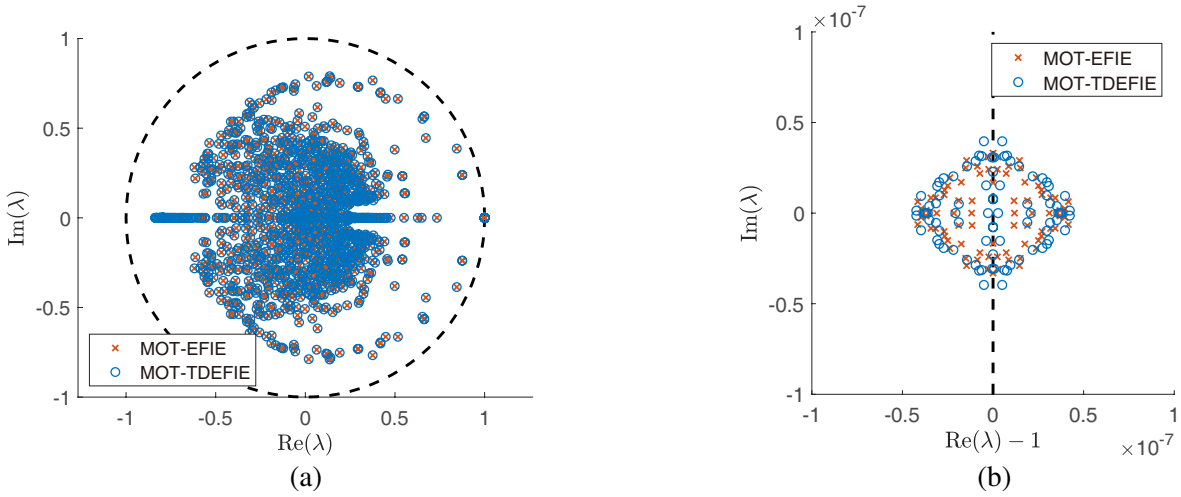

Figure 2. (a) The eigenvalues λ of the MOT-EFIE ($\times$) and MOT-TDEFIE ($\circ$) companion matrices based on the corresponding interaction matrices used to compute the surface current density on the PEC plate in Figure 1(a). (b) The eigenvalues in (a) close to $\lambda = 1$.

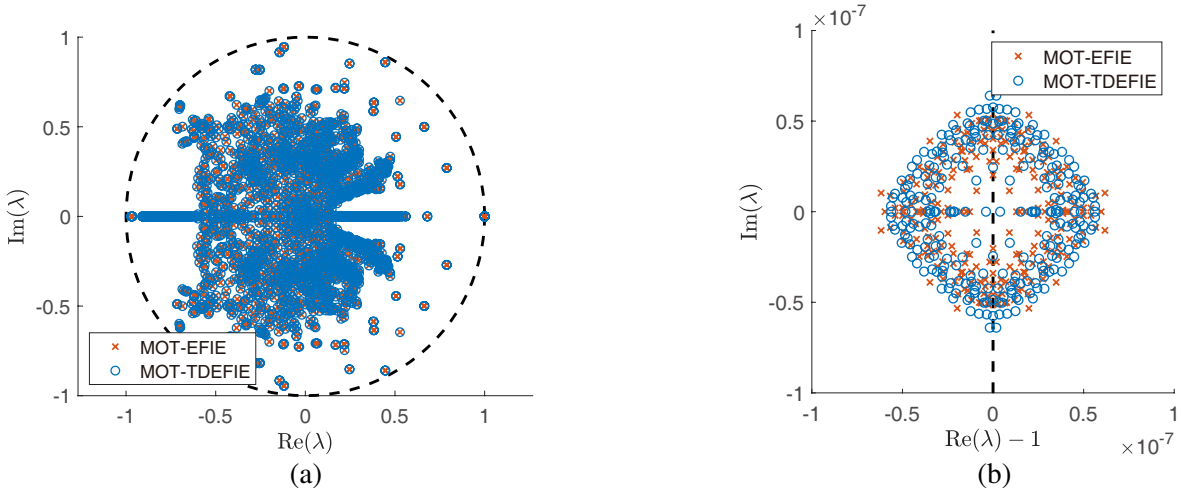

Figure 3. (a) The eigenvalues λ of the MOT-EFIE ($\times$) and MOT-TDEFIE ($\circ$) companion matrices based on the corresponding interaction matrices used to compute the surface current density on the PEC cube in Figure 1(b). (b) The eigenvalues in (a) close to $\lambda = 1$.

the RWG-mesh shown in Figure 4(b). Here, the RWGs can represent a single solenoidal current density indicated by the red arrow. Therefore, we expect to find two eigenvalues close to $\lambda = 1$ in the corresponding companion matrix eigenvalues. The eigenvalues of the companion matrices based on the interaction matrices resulting from the mesh in Figure 4(b) and the solver settings mentioned in Section 4.1 are presented in Figure 4. As expected, we observe two eigenvalues close to $\lambda = 1$ for both the MOT-EFIE and MOT-TDEFIE companion matrices in Figure 4(b).

4.3. Proportionality of $|\alpha|$ to the Square Root Error

For assertion (iii), we mimic finite-precision errors in the calculations of the interaction matrices $\mathbf{Z}_{n-n'}$ by multiplying the $\mathbf{Z}_{n-n'}$ matrix entries by uniformly distributed random numbers in the range $1+[-\sigma, \sigma]$, and we denote the resulting perturbed matrix as $\tilde{\mathbf{Z}}_{n-n'}$. The coefficient σ is a predetermined scaling coefficient. In a similar way, we mimic errors in $\mathbf{Z}^{\partial}_{n-n'}$ and name the resulting matrix $\tilde{\mathbf{Z}}^{\partial}_{n-n'}$. Doing so,

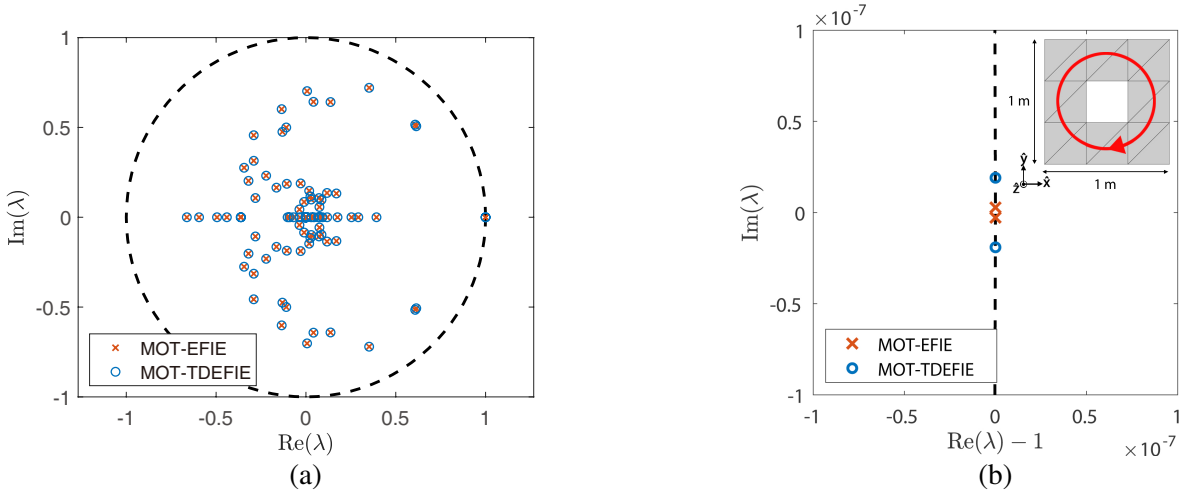

Figure 4. (a) The eigenvalues λ of the MOT-EFIE ($\times$) and MOT-TDEFIE ($\circ$) companion matrices based on the corresponding interaction matrices which are based on the mesh in (b). The red arrow on the mesh in (b) indicates the only solenoidal current density allowed by the RWG discretization. (b) The eigenvalues in (a) close to $\lambda = 1$.

we introduce a relative error σ in all non-zero matrix entries. In accordance with the Lidskii-Vishik-Lyusternik perturbation theory, see Section 3.2, the eigenvalues close to $\lambda = 1$ of the companion matrices based on $\tilde{\mathbf{Z}}_{n-n'}$ and $\tilde{\mathbf{Z}}^{\partial}_{n-n'}$ should exhibit an offset α, where $|\alpha|$ scales as $\mathcal{O}(\sqrt{\sigma})$.

The eigenvalue offset $|\alpha|$, as a function of σ, corresponding to the PEC plate and PEC cube interaction matrices used in Figures 1(a) and 1(b), respectively, are shown in Figures 5 and 6, respectively. As the $\mathcal{O}(\sqrt{\sigma})$ proportionality holds for $\sigma \geq 10^{-14}$, it has allowed us to put the eigenvalues

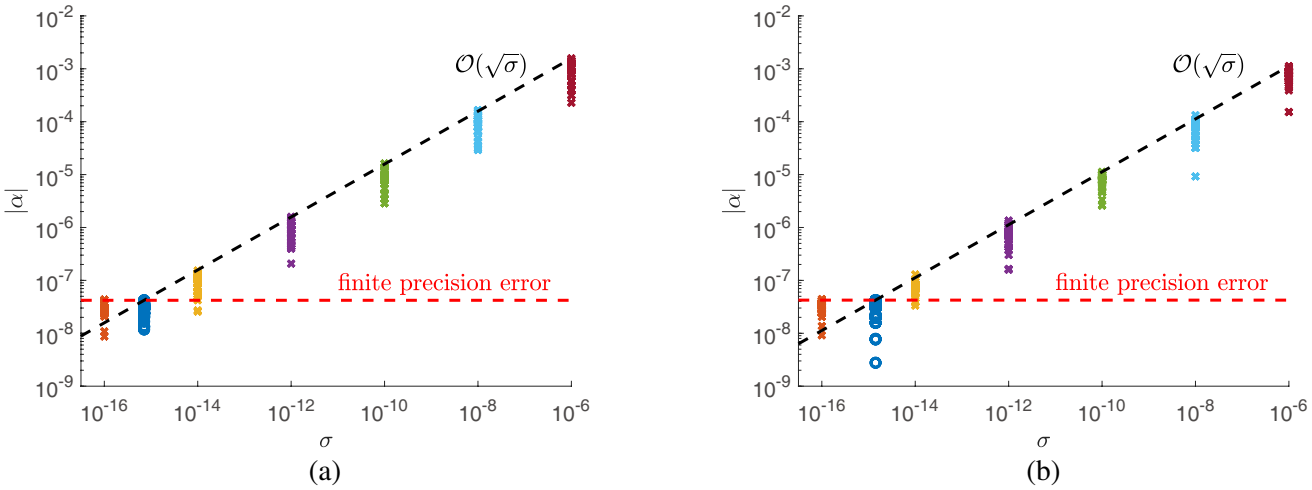

Figure 5. The offset $|\alpha|$ of the (a) MOT-EFIE and (b) MOT-TDEFIE companion matrix eigenvalues close to $\lambda = 1$ as function of σ. The ($\circ$)-markers around $\sigma \approx 10^{-15}$ indicate values that are computed using the companion matrices constructed with the PEC plate interaction matrices, (a) $\mathbf{Z}_{n-n'}$ and (b) $\mathbf{Z}^{\partial}_{n-n'}$, used for the simulation in Figure 1(a). The ($\times$)-markers indicate values that are computed using the companion matrices constructed with the perturbed PEC plate interaction matrices, (a) $\tilde{\mathbf{Z}}_{n-n'}$ and (b) $\tilde{\mathbf{Z}}^{\partial}_{n-n'}$. The black dashed line represents the $\mathcal{O}(\sqrt{\sigma})$ proportionality of $|\alpha|$. The red dashed line indicates the offset $|\alpha|$ due to finite precision arithmetic.

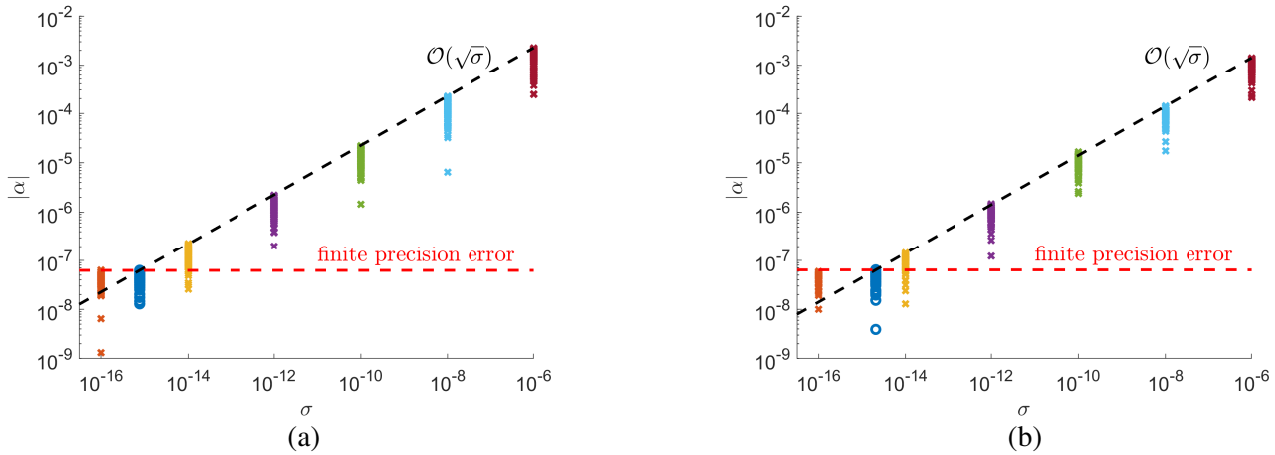

Figure 6. The offset $|\alpha|$ of the (a) MOT-EFIE and (b) MOT-TDEFIE companion matrix eigenvalues close to $\lambda = 1$ as function of σ. The ($\circ$)-markers around $\sigma \approx 10^{-15}$ indicate values that are computed using the companion matrices constructed with the PEC cube interaction matrices, (a) $\mathbf{Z}_{n-n'}$ and (b) $\tilde{\mathbf{Z}}^{\partial}_{n-n'}$, used for the simulation in Figure 1(b). The ($\times$)-markers indicate values that are computed using the companion matrices constructed with the perturbed PEC cube interaction matrices, (a) $\mathbf{Z}_{n-n'}$ and (b) $\tilde{\mathbf{Z}}^{\partial}_{n-n'}$. The black dashed line represents the $\mathcal{O}(\sqrt{\sigma})$ proportionality of $|\alpha|$. The red dashed line indicates the offset $|\alpha|$ due to finite precision arithmetic.

shown in Figures 2(b) and 3(b), i.e., the eigenvalues of the original interaction matrices ($\sigma = 0$), into perspective and have an estimate of the relative error in the calculation of the MOT-EFIE and MOT-TDEFIE interaction matrix entries. The corresponding $|\alpha|$ is indicated by the dark blue ($\circ$)-markers in Figures 5 and 6. The values indicated by ($\circ$)-markers deviate around $\sigma \approx 10^{-15}$. A relative error of this magnitude is typical for the double precision arithmetic in which we have performed the interaction matrix calculations. Therefore, we are convinced that finite precision arithmetic in the MOT-EFIE and MOT-TDEFIE implementations is what prevents the occurrence of a perfect 2×2 Jordan block and causes the Jordan blocks to split. Note that the maximum offset $|\alpha|$ for $\sigma = 10^{-16}$ is of a similar magnitude to the maximum offset for $\sigma = 0$, as indicated by the red dashed line in Figures 5 and 6, as the error is dominated by the finite precision error.

4.4. The Linear-in-Time Solution Instability

For assertion (iv), we recompute the current density shown in Figure 1(a) and Figure 1(b) but replace the interaction matrices in (8) by the perturbed interaction matrices $\tilde{\mathbf{Z}}_{n-n'}$ and $\tilde{\mathbf{Z}}^{\partial}_{n-n'}$ created in Section 4.3. As seen in Section 4.3, the eigenvalue offset increases as $\mathcal{O}(\sqrt{\sigma})$; therefore, we expect a large impact on the current density related to the Jordan blocks.

The MOT-EFIE and MOT-TDEFIE surface current density magnitudes on a PEC plate for different values of the perturbation σ are shown in Figure 7. The MOT-EFIE and MOT-TDEFIE surface current density magnitudes on a PEC cube for different values of σ are shown in Figure 8. The linear-in-time solution instability for $\sigma = 0$ in Figures 7 and 8 is similar to what can be found in literature [10, 11, 15] in the sense that the surface current density magnitude decreases with time until it reaches a point where the surface current density starts to increase linearly with time. The alterations to the interaction matrices seem to have little to no impact on the "correct"-region of the surface current density magnitude in Figures 7 and 8. However, it greatly affects what happens to the linear-in-time solution instability.

The type of surface current density magnitudes allowed by the split Jordan blocks as explained in Section 3.2 can be observed in Figures 7 and 8, i.e., constant, linear-in-time and exponential-in-time surface current density magnitudes. The transition between types due to a shift of the dominant term in Equation (26) is also observed. Additionally, as the Jordan block eigenvalue offset increases with σ, the exponential increase starts at earlier time steps, which is in line with the eigenvalue offset proportionality to $\mathcal{O}(\sqrt{\sigma})$.

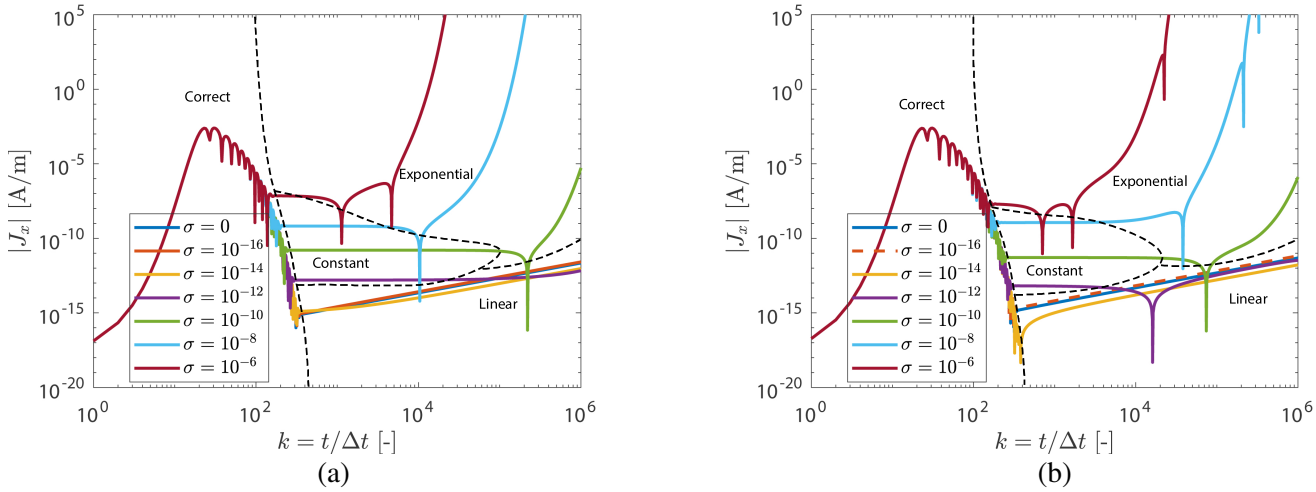

Figure 7. The surface current density magnitude $|J_x|$ at discrete time steps k on the PEC plate as computed in Figure 1(a), but with the perturbed interaction matrices. (a) The MOT-EFIE (8a) solution where $\mathbf{Z}_{n-n'}$ is replaced by $\tilde{\mathbf{Z}}_{n-n'}$. (b) The MOT-TDEFIE (8b) solution where $\mathbf{Z}^{\partial}_{n-n'}$ is replaced by $\tilde{\mathbf{Z}}^{\partial}_{n-n'}$. The regions where the simulation result is "correct", or where it exhibits a "constant", "linear", or "exponential" behavior due to the splitted Jordan block eigenvalues are indicated by dashed boundaries.

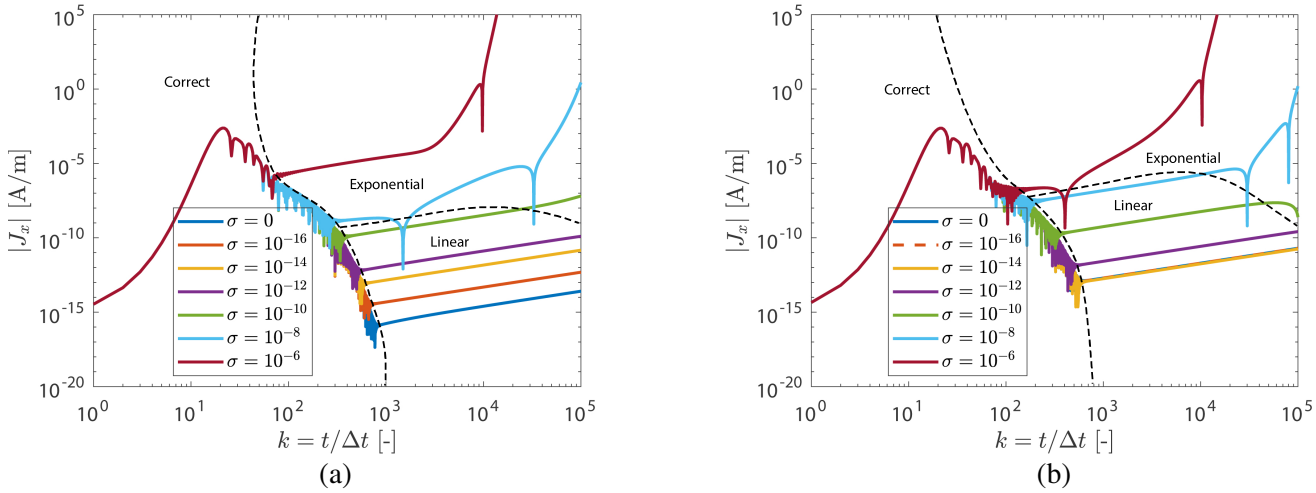

Figure 8. The surface current density magnitude $|J_x|$ at discrete time steps k on the PEC cube as computed in Figure 1(b), but with the perturbed interaction matrices. (a) The MOT-EFIE (8a) solution where $\mathbf{Z}_{n-n'}$ is replaced with $\tilde{\mathbf{Z}}_{n-n'}$. (b) The MOT-TDEFIE (8b) solution where $\mathbf{Z}^{\partial}_{n-n'}$ is replaced with $\tilde{\mathbf{Z}}^{\partial}_{n-n'}$. The regions where the simulation result is "correct", or where it exhibits a "linear", or "exponential" behavior due to the split Jordan block eigenvalues are indicated by dashed boundaries.

Based on these results we can conclude that finite precision effects, combined with the presence of Jordan blocks, are responsible for the instability of these MOT-EFIE and MOT-TDEFIE solvers. Furthermore, we have confirmed for higher σ that the instability is an exponentially increasing surface current density magnitude initially observed as constant or linear-in-time. As the theoretical framework in Section 3.2 has been confirmed with these results, we predict that the $\sigma = 0$ solutions are also exponentially increasing solutions that are initially observed as linear-in-time and will become exponential-in-time solutions around discrete time steps equal to the inverse square root of the finite precision error, i.e., for $k = t/\Delta t \approx 10^8$ time steps in double precision arithmetic.

5. CONCLUSION

The relation between the linear-in-time solution instabilities of the MOT-EFIE and MOT-TDEFIE, based on RWG spatial discretization and linear hat and quadratic spline temporal basis functions, respectively, and their respective null spaces has been studied. A theoretical analysis based on projection matrices demonstrated that the recurrence relation in the interaction matrix elements results in dimension-two Jordan blocks with eigenvalues equal to one in the MOT-EFIE and MOT-TDEFIE companion matrices for each linear combination of RWGs representing a linearly independent solenoidal surface current density. In practice, due to finite precision arithmetic, the recurrence relation is lost, and the eigenvalues in each Jordan block split into two eigenvalues where, according to the Lidskii-Vishik-Lyusternik perturbation theory, the eigenvalue offset is proportional to the square root of the finite precision error. Numerical experiments on PEC scatterers confirmed that: the number of split eigenvalues is equal to twice the number of independent solenoidal surface current densities; the Lidskii-Vishik-Lyusternik perturbation theory holds; finite precision is enough to split the eigenvalues in the Jordan blocks in these MOT-EFIE and MOT-TDEFIE implementations; and the split eigenvalues eventually cause exponentially increasing solution magnitudes that are initially observed as constant and/or linear-in-time but become exponentially increasing at discrete time steps beyond the inverse square root of the error due to finite precision, i.e., $t/\Delta t \approx 10^8$ in double precision arithmetic.

APPENDIX A. ALGEBRAIC MULTIPLICITY

To simplify the determinants $\det(\mathbf{Q}_P - \lambda\mathbf{I})$ and $\det(\mathbf{Q}_P^{\partial} - \lambda^{\partial}\mathbf{I})$, we will split the matrices into 2×2 block matrices, i.e.,

$$\delta = \det\left(\mathbf{Q}_P - \lambda\mathbf{I}\right) = \det\begin{bmatrix} \mathbf{F} & \mathbf{G} \\ \mathbf{K} & \mathbf{L}\left(\lambda, \lambda - 1\right) \end{bmatrix}, \tag{A1a}$$

$$\delta^{\partial} = \det\left(\mathbf{Q}_P^{\partial} - \lambda^{\partial}\mathbf{I}\right) = \det\begin{bmatrix} \mathbf{F}^{\partial} & \mathbf{G}^{\partial} \\ \mathbf{K} & \mathbf{L}\left(\lambda^{\partial}, \lambda^{\partial}\right) \end{bmatrix}, \tag{A1b}$$

where $\mathbf{F} = \mathbf{Q}_{P,1} - \lambda\mathbf{I}$, $\mathbf{F}^{\partial} = \mathbf{Q}_{P,1}^{\partial} - \lambda^{\partial}\mathbf{I}$, $\mathbf{G}$ is a row block-vector containing $\mathbf{Q}_{P,i}$ for $i = 2, \ldots, \ell$ and $\mathbf{Q}_{P,\text{tail}}$ (23a) as blocks; $\mathbf{G}^{\partial}$ is a row block-vector containing $\mathbf{Q}_{P,i}$ for $i = 2, \ldots, \ell^{\partial}$ (23b) as blocks, $\mathbf{K} = [\mathbf{I}, \mathbf{0}, \ldots, \mathbf{0}]^T$; and $\mathbf{L}(\beta_1, \beta_2)$ is a block-matrix where the first lower-block-diagonal is filled with identity matrices $\mathbf{I}$, and the diagonal blocks are filled with matrices $-\beta_1\mathbf{I}$ except for the last block entry, which is filled with the matrix $-\beta_2\mathbf{I}$. If the inverse of $\mathbf{L}^{-1}$ exists, the determinant can be computed using the Schur complement of the matrix, i.e., $\delta = \det(\mathbf{L}(\lambda, \lambda))\det(\mathbf{F} - \mathbf{G}\mathbf{L}^{-1}(\lambda, \lambda - 1)\mathbf{K})$. Owing to the structure of $\mathbf{L}(\beta_1, \beta_2)$, the inverse can be computed using a row division by $-\beta_1$ for the rows containing $-\beta_1\mathbf{I}$, a row division by $-\beta_2$ for the rows containing $-\beta_2\mathbf{I}$, and then applying forward substitution. As $\mathbf{K}$ has $\mathbf{I}$ as the first and only non-zero block entry, we require only the first block-column of $\mathbf{L}^{-1}(\beta_1, \beta_2)$, which is given by

$$\left[\frac{-1}{\beta_1}\mathbf{I},\ \frac{-1}{\beta_1^2}\mathbf{I},\ \ldots,\ \frac{-1}{\beta_1^{M-1}}\mathbf{I},\ \frac{-1}{\beta_2\beta_1^{M-1}}\mathbf{I}\right]^T, \tag{A2}$$

where M indicates that $\mathbf{L}$ is an $M \times M$ block matrix. Multiplying the above block-column by the remaining block-vector the following matrices are defined as

$$\mathbf{G}\mathbf{L}^{-1}(\lambda, \lambda - 1)\mathbf{K} = -\frac{1}{\lambda}\mathbf{Q}_{P,2} - \frac{1}{\lambda^2}\mathbf{Q}_{P,3} - \ldots - \frac{1}{\lambda^{\ell-1}}\mathbf{Q}_{P,\ell} - \frac{1}{(\lambda-1)\lambda^{\ell-1}}\mathbf{Q}_{P,\text{tail}}, \tag{A3a}$$

$$\mathbf{G}^{\partial}\mathbf{L}^{-1}(\lambda^{\partial}, \lambda^{\partial})\mathbf{K} = -\frac{1}{\lambda^{\partial}}\mathbf{Q}_{P,2}^{\partial} - \frac{1}{(\lambda^{\partial})^2}\mathbf{Q}_{P,3}^{\partial} - \ldots - \frac{1}{(\lambda^{\partial})^{\ell-2}}\mathbf{Q}_{P,\ell-1}^{\partial} - \frac{1}{\lambda^{\ell^{\partial}-1}}\mathbf{Q}_{P,\ell}^{\partial}. \tag{A3b}$$

The determinant of $\mathbf{L}$ is also readily computed owing to its matrix structure, i.e., $\det(\mathbf{L}) = \det((-\beta_2)(-\beta_1)^{M-1}\mathbf{I})$. Combining all of the above, we can simplify the determinants in (A1) to

$$\delta = \det\left(-(\lambda-1)(-\lambda)^{\ell-1}\left(\mathbf{Q}_{P,1} - \lambda\mathbf{I} + \sum_{i=2}^{\ell}\frac{1}{\lambda^{i-1}}\mathbf{Q}_{P,i} + \frac{1}{(\lambda-1)\lambda^{\ell-1}}\mathbf{Q}_{P,\text{tail}}\right)\right), \tag{A4a}$$

$$\delta^{\partial} = \det\left((-\lambda^{\partial})(-\lambda^{\partial})^{\ell^{\partial}-2}\left(\mathbf{Q}^{\partial}_{P,1} - \lambda^{\partial}\mathbf{I} + \sum_{i=2}^{\ell^{\partial}}\frac{1}{(\lambda^{\partial})^{i-1}}\mathbf{Q}^{\partial}_{P,i}\right)\right), \tag{A4b}$$

where we have combined the two determinants, i.e., the determinant due to $\det(\mathbf{L})$ and the other determinant due to $\det(\mathbf{F}-\mathbf{G}\mathbf{L}^{-1}\mathbf{K})$, into a single determinant of a matrix polynomial. As all matrices are multiplied by the same eigenvalue power and all companion matrices multiplied by the same matrix inverse, see Equations (23a), (23b), further simplification of the above equations is possible, i.e.,

$$\delta = \det\left(\begin{bmatrix}\mathbf{Z}_0^{\boldsymbol{\theta\theta}} & \mathbf{Z}_0^{\boldsymbol{\theta\psi}}\\ \mathbf{Z}_0^{\boldsymbol{\psi\theta}} & \mathbf{Z}_0^{\boldsymbol{\psi\psi}}\end{bmatrix}^{-1}\right)\det\left((-1)^{\ell+1}\left((\lambda-1)\sum_{i=0}^{\ell}\begin{bmatrix}\mathbf{Z}_i^{\boldsymbol{\theta\theta}} & \mathbf{Z}_i^{\boldsymbol{\theta\psi}}\\ \mathbf{Z}_i^{\boldsymbol{\psi\theta}} & \mathbf{Z}_i^{\boldsymbol{\psi\psi}}\end{bmatrix}\lambda^{\ell-i} + \begin{bmatrix}\mathbf{0} & \mathbf{0}\\ \mathbf{0} & \mathbf{Z}_{\text{tail}}^{\boldsymbol{\psi\psi}}\end{bmatrix}\right)\right), \tag{A5a}$$

$$\delta^{\partial} = \det\left(\begin{bmatrix}\mathbf{Z}_0^{\partial\boldsymbol{\theta\theta}} & \mathbf{Z}_0^{\partial\boldsymbol{\theta\psi}}\\ \mathbf{Z}_0^{\partial\boldsymbol{\psi\theta}} & \mathbf{Z}_0^{\partial\boldsymbol{\psi\psi}}\end{bmatrix}^{-1}\right)\det\left((-1)^{\ell^{\partial}}\left(\sum_{i=0}^{\ell^{\partial}}\begin{bmatrix}\mathbf{Z}_i^{\partial\boldsymbol{\theta\theta}} & \mathbf{Z}_i^{\partial\boldsymbol{\theta\psi}}\\ \mathbf{Z}_i^{\partial\boldsymbol{\psi\theta}} & \mathbf{Z}_i^{\partial\boldsymbol{\psi\psi}}\end{bmatrix}\lambda^{\ell^{\partial}-i}\right)\right). \tag{A5b}$$

In finding the solutions to $\delta = 0$ and $\delta^{\partial} = 0$, the determinant of the matrix inverse in the above expressions is irrelevant as an invertible matrix always has a non-zero determinant. To find the eigenvalues for which the second determinants in Equations (A5a), (A5b) equals zero, it is important to note the recurrence relation in the matrix elements, owing to the piecewise constant derivatives of the time-expansion functions $\dot{T}_0$ (7a) and $\ddot{T}_0^{\partial}$ (7b), i.e.,

$$\mathbf{Z}_n^{\mathbf{xx}'} = \mathbf{A}_n^{\mathbf{xx}'} - \mathbf{A}_{n-1}^{\mathbf{xx}'} + \mathbf{B}_n^{\mathbf{xx}'}, \tag{A6a}$$

$$\mathbf{Z}_n^{\partial\mathbf{xx}'} = \frac{1}{2}\mathbf{A}_n^{\mathbf{xx}'} - \mathbf{A}_{n-1}^{\mathbf{xx}'} + \frac{1}{2}\mathbf{A}_{n-2}^{\mathbf{xx}'} + \mathbf{B}_n^{\partial\mathbf{xx}'}, \tag{A6b}$$

where the matrix elements of $\mathbf{A}_i^{\mathbf{xx}'}$ are

$$A_n^{\mathbf{xx}'}(m,m') = \begin{cases} 0 & \text{for } n<0\\ \mu_0\displaystyle\int_{\Gamma_m}\mathbf{x}_m(\mathbf{r})\cdot\int_{\Gamma_{m'}}\frac{\mathbf{x}_{m'}(\mathbf{r}')}{4\pi R}\,\mathrm{d}A'\mathrm{d}A, & \text{for } nc\Delta t \le R < (n+1)c\Delta t\\ 0 & \text{otherwise,}\end{cases} \tag{A7}$$

and

$$\mathbf{B}_n^{\mathbf{xx}'} = \phi(\mathbf{x},\mathbf{x}',T_0(\tau_n)), \quad \mathbf{B}_n^{\partial\mathbf{xx}'} = \dot{\phi}(\mathbf{x},\mathbf{x}',T_0^{\partial}(\tau_n)). \tag{A8a,b}$$

In the above expressions $\mathbf{x}$ and $\mathbf{x}'$ can be replaced with $\boldsymbol{\theta}$ and $\boldsymbol{\psi}$ to obtain the recurrence relations for the interaction matrix blocks in Equations (A5a), (A5b). Substituting the recurrence relations in Equations (A6a), (A6b) in the summation expressions in (A5a), (A5b) allows the following factorizations

$$\sum_{i=0}^{\ell}\mathbf{Z}_i^{\mathbf{xx}'}\lambda^{\ell-i} = (\lambda-1)\sum_{i=0}^{\ell-1}\mathbf{A}_i^{\mathbf{xx}'}\lambda^{\ell-1-i} + \sum_{i=0}^{\ell}\mathbf{B}_i^{\mathbf{xx}'}\lambda^{\ell-i}, \tag{A9a}$$

$$\sum_{i=0}^{\ell^{\partial}}\mathbf{Z}_i^{\partial\mathbf{xx}'}\lambda^{\ell^{\partial}-i} = \frac{1}{2}(\lambda-1)^2\sum_{i=0}^{\ell^{\partial}-2}\mathbf{A}_i^{\partial\mathbf{xx}'}\lambda^{\ell^{\partial}-2-i} + \sum_{i=0}^{\ell^{\partial}}\mathbf{B}_i^{\mathbf{xx}'}\lambda^{\ell^{\partial}-i}. \tag{A9b}$$

The interaction matrix summation in Equation (A5a) was already multiplied by $(\lambda-1)$, so we arrive at matrix polynomials with a common factor $(\lambda-1)^2$ for both the summations in Equation (A5a) and

Equation (A5b). The common factor can be isolated from the polynomials, resulting in the following factorization

$$\left(\sum_{i=0}^{\ell-1}\begin{bmatrix}\mathbf{A}_i^{\boldsymbol{\theta\theta}} & (\lambda-1)^2\mathbf{A}_i^{\boldsymbol{\theta\psi}}\\ \mathbf{A}_i^{\boldsymbol{\psi\theta}} & (\lambda-1)^2\mathbf{A}_i^{\boldsymbol{\psi\psi}}\end{bmatrix}\lambda^{\ell-1-i}+\begin{bmatrix}\mathbf{0} & \mathbf{0}\\ \mathbf{0} & (\lambda-1)\sum_{i=0}^{\ell}\mathbf{B}_i^{\boldsymbol{\psi\psi}}\lambda^{\ell-i}+\mathbf{Z}_{\text{tail}}^{\boldsymbol{\psi\psi}}\end{bmatrix}\right)\begin{bmatrix}(\lambda-1)^2\mathbf{I}^{\Theta} & \mathbf{0}\\ \mathbf{0} & \mathbf{I}^{\Psi}\end{bmatrix}, \tag{A10a}$$

$$\left(\frac{1}{2}\sum_{i=0}^{\ell^{\partial}-2}\begin{bmatrix}\mathbf{A}_i^{\partial\boldsymbol{\theta\theta}} & (\lambda^{\partial}-1)^2\mathbf{A}_i^{\partial\boldsymbol{\theta\psi}}\\ \mathbf{A}_i^{\partial\boldsymbol{\psi\theta}} & (\lambda^{\partial}-1)^2\mathbf{A}_i^{\partial\boldsymbol{\psi\psi}}\end{bmatrix}\lambda^{\ell^{\partial}-2-i}+\begin{bmatrix}\mathbf{0} & \mathbf{0}\\ \mathbf{0} & \sum_{i=0}^{\ell^{\partial}}\mathbf{B}_i^{\partial\boldsymbol{\psi\psi}}\lambda^{\ell^{\partial}-i}\end{bmatrix}\right)\begin{bmatrix}(\lambda^{\partial}-1)^2\mathbf{I}^{\Theta} & \mathbf{0}\\ \mathbf{0} & \mathbf{I}^{\Psi}\end{bmatrix}, \tag{A10b}$$

where the superscripts of the identity matrices indicate their respective dimensions. Since the determinant of the product of two square matrices can be written as the product of the determinants of each matrix, a solution to both $\delta = 0$ and $\delta^{\partial} = 0$ is

$$\det\left(\begin{bmatrix}(\lambda^{(\partial)}-1)^2\mathbf{I}^{\Theta} & \mathbf{0}\\ \mathbf{0} & \mathbf{I}^{\Psi}\end{bmatrix}\right) = 0 \Leftrightarrow \left((\lambda^{(\partial)}-1)^2\right)^{\Theta} = 0. \tag{A11}$$

APPENDIX B. GEOMETRIC MULTIPLICITY AND JORDAN BLOCK DIMENSION

To determine the number of Jordan blocks corresponding to $\lambda = 1$ in the JCF of projected companion matrices $\mathbf{Q}_P$ (23a) and $\mathbf{Q}_P^{\partial}$ (23b), we have to find all linearly independent vectors $\mathbf{v}$ and $\mathbf{v}^{\partial}$ for which

$$(\mathbf{Q}_P - \mathbf{I})\,\mathbf{v} = \mathbf{0}, \quad \left(\mathbf{Q}_P^{\partial} - \mathbf{I}\right)\mathbf{v}^{\partial} = \mathbf{0}, \tag{B1a,b}$$

holds. If we formulate the vector as

$$\mathbf{v} = \left[\mathbf{v}_1, \ldots, \mathbf{v}_{\ell}, \mathbf{v}_{\text{tail}}\right]^T, \quad \mathbf{v}^{\partial} = \left[\mathbf{v}_1^{\partial}, \ldots, \mathbf{v}_{\ell-1}^{\partial}, \mathbf{v}_{\ell}^{\partial}\right]^T, \tag{B2a,b}$$

then

$$\mathbf{v}_1 = \cdots = \mathbf{v}_{\ell} = \mathbf{0}, \quad \mathbf{v}_1^{\partial} = \cdots = \mathbf{v}_{\ell}^{\partial}, \tag{B3a,b}$$

owing to the identity-block row structure in $(\mathbf{Q}_P - \mathbf{I})$ and $(\mathbf{Q}_P^{\partial} - \mathbf{I})$, respectively.

Equation (B1a) can be simplified to

$$\begin{bmatrix}\mathbf{0} & \mathbf{0}\\ \mathbf{0} & \mathbf{Z}_{\text{tail}}^{\boldsymbol{\psi\psi}}\end{bmatrix}\begin{bmatrix}\mathbf{v}_{\text{tail}}^{\boldsymbol{\theta}}\\ \mathbf{v}_{\text{tail}}^{\boldsymbol{\psi}}\end{bmatrix} = \mathbf{0}, \tag{B4}$$

where we have split $\mathbf{v}_{\text{tail}}$ in two subvectors $\mathbf{v}_{\text{tail}}^{\boldsymbol{\theta}}$ and $\mathbf{v}_{\text{tail}}^{\boldsymbol{\psi}}$. The matrix $\mathbf{Z}_{\text{tail}}^{\boldsymbol{\psi\psi}}$ (22) is invertible, see Appendix C. This implies $\mathbf{v}_{\text{tail}}^{\boldsymbol{\psi}} = \mathbf{0}$, and we can define Θ linearly independent eigenvectors $\mathbf{v}$. Consequently, the geometric multiplicity of $\lambda = 1$ in the JCF of $\mathbf{Q}_P$ is Θ.

Equation (B1b) together with Equation (B3b) can be simplified to

$$\sum_{i=0}^{\ell^{\partial}}\begin{bmatrix}\mathbf{Z}_i^{\partial\boldsymbol{\theta\theta}} & \mathbf{Z}_i^{\partial\boldsymbol{\theta\psi}}\\ \mathbf{Z}_i^{\partial\boldsymbol{\psi\theta}} & \mathbf{Z}_i^{\partial\boldsymbol{\psi\psi}}\end{bmatrix}\mathbf{v}_1^{\partial} = \begin{bmatrix}\mathbf{0} & \mathbf{0}\\ \mathbf{0} & \sum_{i=0}^{\ell^{\partial}}\mathbf{B}_i^{\partial\boldsymbol{\psi\psi}}\end{bmatrix}\begin{bmatrix}\mathbf{v}_1^{\partial\boldsymbol{\theta}}\\ \mathbf{v}_1^{\partial\boldsymbol{\psi}}\end{bmatrix} = \mathbf{0}, \tag{B5}$$

using the recurrence relation in Equation (A6b). The matrix $\sum_{i=0}^{\ell^{\partial}}\mathbf{B}_i^{\partial\boldsymbol{\psi\psi}}$ is invertible, see Appendix C. This implies $\mathbf{v}_1^{\partial\boldsymbol{\psi}} = \mathbf{0}$, and we can define Θ linearly independent eigenvectors $\mathbf{v}^{\partial}$. So, the geometric multiplicity of $\lambda = 1$ in the JCF of $\mathbf{Q}_P^{\partial}$ is Θ.

Since $\lambda = 1$ has geometric multiplicity Θ and algebraic multiplicity 2Θ, the associated eigenspace is incomplete. To determine the size of each of the Jordan blocks for this subspace, we require the generalized eigenvectors $\mathbf{v}^{+}$ and $\mathbf{v}^{\partial+}$ [22], which should satisfy

$$(\mathbf{Q}_P - \mathbf{I})\,\mathbf{v}^{+} = \mathbf{v}, \quad \left(\mathbf{Q}_P^{\partial} - \mathbf{I}\right)\mathbf{v}^{\partial+} = \mathbf{v}^{\partial}, \tag{B6a,b}$$

for each independent eigenvector $\mathbf{v}$ or $\mathbf{v}^{\partial+}$, respectively. The solutions to the above equations can be found by exploiting the recurrence relations in Equation (A6) and are given by

$$\mathbf{v}^{+} = \gamma\mathbf{v} + [\mathbf{v}_{\text{tail}}, \ldots, \mathbf{v}_{\text{tail}}]^{T}, \quad \mathbf{v}^{\partial+} = \gamma^{\partial}\mathbf{v}^{\partial} - \mathbf{D}\mathbf{v}^{\partial}, \tag{B7a,b}$$

where $\mathbf{D}$ is a diagonal matrix with subsequent diagonal elements $[0, 1, \ldots, \ell^{\partial} - 1]$, and one is free to choose a value for the scaling coefficients γ and γ^{∂}. Equation (B7) implies that for each of the Θ independent eigenvectors we find an associated and independent generalized eigenvector. Therefore, the dimension of each of the associated Jordan blocks is two.

APPENDIX C. INVERTIBLE MATRICES

The matrices $\mathbf{Z}_{\text{tail}}^{\psi\psi}$ (22) and $\sum_{i=0}^{\ell^{\partial}} \mathbf{B}_{i}^{\partial\psi\psi}$ (A8) are equal except for a scaling coefficient, i.e., the elements of the matrices are defined as

$$\sum_{i=0}^{\ell^{\partial}} \mathbf{B}_{i}^{\partial\psi\psi}(p, p') = \dot{\phi}(\boldsymbol{\psi}_{p}, \boldsymbol{\psi}_{p'}, 1) = \frac{1}{\Delta t}\mathbf{Z}_{\text{tail}}^{\psi\psi}(p, p'). \tag{C1}$$

The one in the above expression represents a constant unit function over the entire time domain and is the result of the summation of the temporal basis functions T_{0}^{∂} (7b), i.e., $\sum_{n} T_{0}^{\partial}(\tau_{n}) = 1$. As the matrices are scaled versions of one another, if $\mathbf{Z}_{\text{tail}}^{\psi\psi}$ is invertible then $\sum_{i=0}^{\ell^{\partial}} \mathbf{B}_{i}^{\partial\psi\psi}$ is also invertible.

The matrix $\mathbf{Z}_{\text{tail}}^{\psi\psi}$ (22) is real and symmetric and for $\mathbf{Z}_{\text{tail}}^{\psi\psi}$ to be invertible

$$\mathbf{x}^{T}\mathbf{Z}_{\text{tail}}^{\psi\psi}\mathbf{x} > 0 \ \text{ for } \ \mathbf{x} \neq \mathbf{0}, \tag{C2}$$

needs to hold. Because

$$\nabla_{s}' \cdot \sum_{p'=1}^{\Psi} x_{p'}\boldsymbol{\psi}_{p'} = 0 \ \text{ if and only if } \ x_{p'} = 0 \ \text{ for } \ p' = 1, \ldots, \Psi, \tag{C3}$$

as $\boldsymbol{\psi}_{p'}$ are linearly independent non-solenoidal basis functions, and a linear combination of $\boldsymbol{\psi}_{p'}$ can never represent a solenoidal surface current density due to the invertibility of the projection matrix $\mathbf{P}$ in Equation (16), the integrand is strictly positive, which implies that

$$\mathbf{x}^{T}\mathbf{Z}_{\text{tail}}^{\psi\psi}\mathbf{x} = \Delta t \int\int \frac{1}{\epsilon_{0}} \frac{\left(\nabla_{s}' \cdot \sum_{p'=1}^{\Psi} x_{p'}\boldsymbol{\psi}_{p'}\right)^{2}}{4\pi R} \mathrm{d}A'\mathrm{d}A > 0 \ \text{ for } \ \mathbf{x} \neq \mathbf{0}. \tag{C4}$$

Thus $\mathbf{Z}_{\text{tail}}^{\psi\psi}$ and therefore $\sum_{i=0}^{\ell^{\partial}} \mathbf{B}_{i}^{\partial\psi\psi}$ are invertible.

REFERENCES

1. Jin, J.-M. and S. Yan, "Multiphysics modeling in electromagnetics," *IEEE Antennas and Propagation Magazine*, 14–26, April 2019.
2. Sankaran, K., "Are you using the right tools in computational electromagnetics?" *Engineering Reports*, Vol. 1, No. 3, 1–19, 2019.
3. Miller, E. K., "A selective survey of computational electromagnetics," *IEEE Transactions on Antennas and Propagation*, Vol. 36, No. 9, 1281–1305, 1988.
4. Weile, D. S., J. Li, D. A. Hopkins, and C. Kerwein, "New trends in time-domain integral equations," *New Trends in Computational Electromagnetics*, Ö. Ergül, ed., 1st Edition, Ch. 5, 207–233, SciTech Publishing, London, 2019.
5. Liu, Y. and E. Michielssen, "Parallel fast time-domain integral-equation methods for transient electromagnetic analysis," *Parallel Algorithms in Computational Science*, A. Grama and A. H. Sameh (eds.), 1st Edition, Ch. 2.8, 347–379, Cham, Switzerland, Birkhäuser, 2020.

6. Poggio, A. and E. Miller, "Integral equation solutions of three-dimensional scattering problems," *Computer Techniques for Electromagnetics*, R. Mittra (ed.), 1st Edition, Ch. 4, 159–264, Pergamon Press, Oxford, 1973.
7. Andriulli, F. P., K. Cools, F. Olyslager, and E. Michielssen, "Time domain Calderón identities and their application to the integral equation analysis of scattering by PEC objects. Part II: Stability," *IEEE Transactions on Antennas and Propagation*, Vol. 57, No. 8, 2365–2375, 2009.
8. Shanker, B., M. Lu, J. Yuan, and E. Michielssen, "Time domain integral equation analysis of scattering from composite bodies via exact evaluation of radiation fields," *IEEE Transactions on Antennas and Propagation*, Vol. 57, No. 5, 1506–1520, 2009.
9. Van 't Wout, E., D. R. van der Heul, H. van der Ven, and C. Vuik, "The influence of the exact evaluation of radiation fields in finite precision arithmetic on the stability of the time domain integral equation method," *IEEE Transactions on Antennas and Propagation*, Vol. 61, No. 12, 6064–6074, 2013.
10. Van 't Wout, E., D. R. van der Heul, H. van der Ven, and C. Vuik, "Stability analysis of the marching-on-in-time boundary element method for electromagnetics," *Journal of Computational and Applied Mathematics*, Vol. 294, 358–371, 2016.
11. Weile, D. S., G. Pisharody, N. W. Chen, B. Shanker, and E. Michielssen, "A novel scheme for the solution of the time-domain integral equations of electromagnetics," *IEEE Transactions on Antennas and Propagation*, Vol. 52, No. 1, 283–295, 2004.
12. Tian, X. and G. Xiao, "Time-domain augmented electric field integral equation for a robust marching on in time solver," *IET Microwaves, Antennas and Propagation*, Vol. 8, No. 9, 688–694, 2014.
13. Cools, K., F. P. Andriulli, F. Olyslager, and E. Michielssen, "Time domain Calderón identities and their application to the integral equation analysis of scattering by PEC objects. Part I: Preconditioning," *IEEE Transactions on Antennas and Propagation*, Vol. 57, No. 8, 2352–2364, 2009.
14. Beghein, Y., K. Cools, and F. P. Andriulli, "A DC stable and large-time step well-balanced TDEFIE based on quasi-helmholtz projectors," *IEEE Transactions on Antennas and Propagation*, Vol. 63, No. 7, 3087–3097, 2015.
15. Dely, A., F. P. Andriulli, and K. Cools, "Large time step and DC stable TD-EFIE discretized with implicit Runge-Kutta methods," *IEEE Transactions on Antennas and Propagation*, Vol. 68, No. 2, 976–985, 2020.
16. Dodson, S., S. Walker, and M. Bluck, "Implicitness and stability of time domain integral equation scattering analyses," *The Applied Computational Electromagnetics Society*, Vol. 13, No. 3, 291–301, 1998.
17. Wilton, D. R., S. M. Rao, and A. W. Glisson, "Electromagnetic scattering by surfaces of arbitrary shape," *IEEE Transactions on Antennas and Propagation*, Vol. 30, No. 3, 409–418, 1982.
18. Horn, R. A. and C. R. Johnson, *Matrix Analysis*, 2nd Edition, Cambridge University Press, New York, 2013.
19. Moro, J., J. V. Burke, and M. L. Overton, "On the Lidski-Vishik-Lyusternik perturbation theory for eigenvalues of matrices with arbitrary Jordan structure," *SIAM Journal on Matrix Analysis and Applications*, Vol. 18, No. 4, 793–817, 1997.
20. Vechinski, D. and S. Rao, "A stable procedure to calculate the transient scattering by conducting surfaces of arbitrary shape," *IEEE Transactions on Antennas and Propagation*, Vol. 40, No. 6, 661–665, 1992.
21. Andriulli, F. P., K. Cools, I. Bogaert, and E. Michielssen, "On a well-conditioned electric field integral operator for multiply connected geometries," *IEEE Transactions on Antennas and Propagation*, Vol. 61, No. 4, 2077–2087, 2013.
22. Bronson, R., G. B. Costa, and J. T. Saccoman, "Appendix A — Jordan canonical forms," *Linear Algebra*, 3rd Edition, 379–411, Academic Press, 2014.